SAND2000-0983J

INSENTROPIC COMPRESSION OF SOLIDS USING PULSED MAGNETIC LOADING

C.A. Hall, J.R. Asay, W.A. Stygar, R.B. Spielman, S.E. Rosenthal, and M.D. Knudson
*Sandia National Laboratories**

D. Reisman, A. Toor, R. Cauble
Lawrence Livermore National Laboratories

D.B. Hayes
Tijeras, NM 87059

Abstract

Shock loading techniques are often used to determine material response along a specific pressure loading curve referred to as the Hugoniot. However, many technological and scientific applications require accurate determination of dynamic material response that is off-Hugoniot, covering large regions of the equation-of-state surface. Unloading measurements from the shocked state provide off-Hugoniot information, but experimental techniques for measuring compressive off-Hugoniot response have been limited. A new pulsed magnetic loading technique is presented which provides previously unavailable information on isentropic loading of materials to pressures of several hundred kbar. This smoothly increasing pressure loading provides a good approximation to the high-pressure material isentrope centered at ambient conditions. The approach uses high current densities to create ramped magnetic loading to a few hundred kbar over time intervals of 100-200 ns. The method has successfully determined the isentropic mechanical response of copper to about 200 kbar and has also been used to evaluate the kinetics of the alpha-epsilon phase transition occurring in iron at 130 kbar. With refinements in progress, the method shows promise for performing isentropic compression experiments to multi-Mbar pressures.

Introduction

Planar shock compression is the principal tool used to determine the high-pressure equation-of-state (EOS) of materials[1]. In these methods, flat specimens are subjected to one-dimensional shocks with durations of a few nanoseconds to several microseconds. Traditional sources for generating planar shock loading include explosive lenses or high velocity smooth-bore launchers. In recent years, intense lasers and pulsed power techniques have been developed for these applications. The properties of steady shock waves produced under planar loading, such as shock velocity and particle velocity behind the shock, are typically measured and then used with the conservation equations[1] for steady waves to determine a pressure-volume-energy datum on the equation-of-state surface (EOS). The locus of end states obtained by passing steady shocks through a material at ambient conditions defines a curve on the EOS surface referred to as the principal Hugoniot. Although shock wave methods are useful for obtaining EOS information, the Hugoniot curve is not sufficient to determine the complete thermodynamic EOS needed in many applications.

Isothermal and isentropic loading, can also be used for EOS measurements. The relationship between the isotherm, the Hugoniot produced by shock loading of a fluid (strength effects are ignored for this discussion), and the room temperature isentrope in an aluminum fluid from SESAME EOS tables is shown in Fig. 1. The isentrope, which lies between the isotherm and the Hugoniot, is the response obtained from continuous adiabatic and reversible compression and release. The isotherm, typically measured with hydrostatic pressure vessels or diamond anvil cells (DAC), is determined through slow

DISCLAIMER

DISCLAIMER

Portions of this document may be illegible in electronic image products. Images are produced from the best available original document.

compression at constant temperature. For most solids, isentropic compression and isothermal compression produce nearly equal strains to high pressures, differing by only about 1% in aluminum at 6 Mbar as an example. Although shock compression is also adiabatic, it is highly irreversible. Even so, the isentrope and the Hugoniot are second-order tangent at the initial state[2], so the measurement of an isentropic curve is a good representation of the Hugoniot to pressures of a few hundred kbar in many materials. This will be discussed in more detail in a later section, but it should be pointed out that the above discussion strictly applies to fluid response; the response of solids is complicated by elastic stresses that produce a non-hydrostatic state of stress.

While it is difficult to produce states of isentropic compression with static methods, it is possible to produce continuous, adiabatic loading to pressures of several tens of kbar with dynamic techniques. The loading is not perfectly isentropic because it is not strictly reversible for several reasons. In fluids, real material effects, such as viscous dissipation, non-equilibrium phase transformations, or chemical reactions will result in entropy generation. Solids can only support finite deviatoric elastic stresses, and work done by plastic deformation also constitutes irreversible behavior. Even though the entropy contribution from these effects is generally small[2], the dynamic response of materials under continuous adiabatic loading should strictly be referred to as quasi-isentropic. For historical reasons[3], and because the entropy increase due to these irreversible effects is often small[2] for a wide class of materials, ramp loading experiments will be referred to as Isentropic Compression Experiments (ICE) in the following sections.

Flat-plate projectile impact techniques provide a way to produce precise loading of solids and liquids to high pressure. In these techniques, a flat plate is launched to high velocity and impacts a second flat plate. Each experiment produces a unique state of pressure, volume and internal energy, which can be determined through application of conservation of mass, momentum and energy for steady waves usually called the Hugoniot jump conditions.

Plate impact techniques are not well suited for producing smoothly increasing loading over 100's of ns required for ICE because of their propensity to produce shocks. With some limitations, however, gun techniques have been successful for ICE measurements. Barker and Hollenbach[4] were among the first with well-controlled, smooth ramp loading of solids using projectile impact technologies to study EOS properties. These measurements were made using fused silica, which has a negative curvature, longitudinal stress-uniaxial strain-loading path to approximately 30 kbar. The negative curvature results in a decreasing sound velocity with increasing stress so that as a shock traverses fused silica it broadens into a ramp. The rise time of the transmitted ramp can be controlled by the thicknesses of the fused silica. The generator can therefore be used to produce initial ramp loading in a test sample by placing the sample on the rear of a fused silica buffer. These techniques have been use for isentropic EOS measurements, and for studying the dependence of mechanical properties on loading rate[4,5].

Since fused silica ramp generators are limited to stresses of about 30 kbar, other materials were necessary to generate ramp waves to higher pressure. The principal requirement is that the curvature of the loading path be concave downward so that stable shock waves

cannot be supported and a shock will broaden into a ramp during passage. Some ceramic materials have this characteristic, due to the open nature of the crystal structure. Asay and Chhabildas[6] used a commercially available ceramic to determine the principal isentrope for aluminum to pressures of about 200 kbar.

To extend ramp loading to even higher pressures, Barker developed a method for producing quasi-isentropic loading with direct plate impact methods[3]. In this approach, a particle sedimentation technique was used to produce an impactor plate with a gradation in density. Through careful control of the density profile (low density at the impact side, increasing to high density at the rear surface), he was able to produce relatively smooth ramp loading to high pressure with only a small initial shock. The technique has not seen widespread use because of the difficulty in reproducibly manufacturing graded density impactors. Chhabildas et al[7] developed a layered-plate technique for introducing a series of small, staged shocks into samples that approximated the graded density. This technique provided better density control so that initial input conditions could be closely replicated, but did not introduce the desired smoothly increasing, continuous sample loading.

Hawke et al[8]. were among the first to use relatively slow explosively driven pulse power techniques for EOS measurements in hydrogen. A new capability for producing isentropic compression using fast pulsed power as the energy source is currently being developed on the Z Accelerator[9] at Sandia National Laboratories in Albuquerque, NM. This drive source offers many advantages over previous experimental techniques. These include (1) introduction of a smoothly increasing pressure load into a sample without the

initial low-level shocks produced by impact, (2) the ability to investigate several samples experiencing essentially identical loading during a single experiment, and (3) a loading profile that can be tailored in pressure or risetime to meet experimental requirements. In the context of the earlier discussion, the resulting loading condition is closer to a true isentropic measurement in materials.

Specific examples of this new capability will be discussed, including ICE measurements of copper compressed to about 200 kbar and ICE measurements of iron that demonstrate the ability to detect and study a solid-solid phase transition. The latter data provide information on the bcc-hcp phase transition kinetics that will be discussed and compared with results from previous investigations.

Experimental Configuration for ICE Measurements

The *Z* Accelerator at Sandia National Laboratories is a low inductance pulsed power generator capable of capacitively storing 11.6 MJ of electrical energy. A schematic of the accelerator is shown in Fig. 2. The accelerator uses a combination of fast switches and transmission lines to deliver about 20 MA of electrical current to inductive loads over time scales of 100 ns in its present configuration, and about 200 ns in a projected future configuration. The machine has been used for a variety of applications, including acceleration of electrons and ions for inertial confinement fusion applications and generation of intense x-ray environments through *Z*-pinch driven plasma implosions[9]. For the present application, it is used as a current source to generate time-varying

magnetic fields between the anode and cathode that continuously load planar specimens under study.

Our goals for isentropic compression experiments with this technique to allow 1-2% accuracy in pressure-volume material response curves can be summarized as follows:

- One-dimensional, planar pressure loading, uniform to 0.5%, over a diameter sufficiently large to prevent edge effects from influencing the measurement over the experimental timescales.
- Smoothly increasing pressure loading applied to a sample surface over times of 100-200 ns to prevent shock formation within the sample.
- Propagation of compression waves into undisturbed material at a known initial state for accurate application of the wave analysis.
- The ability to investigate of a minimum of two sample thicknesses experiencing "identical" loading for determination of lagrangian wave speed.
- Ability to obtain time resolved particle velocity histories in the rear surface of specimens to achieve approximately 1% accuracy in wavespeeds.

The principle that allows pulsed power to apply shockless loading to EOS samples is illustrated in Figure 3a. Low inductance loads were designed for the Z accelerator and fielded at the center of Z's radially converging magnetically-insulated transmission lines. The total vacuum section inductance was typically 11nH. The EOS specimens were mounted in the load's current carrying surfaces at a radius of 1–2 cm relative to the axis of the machine. A typical load current waveform is shown in Figure 3b.

The applied current, I, results in a local current density, J, at each point on the surface of the anode and cathode. The local current density produces a local magnetic field. The magnetic pressure produced on the surface of the conductors is given by

$$P_{mag}(t) = (1/2\mu_0)\, B^2\,(t),$$

$$= (\mu_0/2)[I/w]^2 \quad \text{MKS}, \qquad (1)$$

where the magnetic pressure, P_{mag}, is in Pascals for MKS units, μ_0 is the permeability of free space ($4\pi \times 10^{-7}$ N/A^2), B is the magnetic field, and I is the applied current in amps. For a constant width conductor, the current density is the applied field divided by the width, w, of the conducting area. For a cylindrically converging geometry, the width w is the circumference of a circle at the location of interest.

If a sample is placed in either the anode or cathode and current is allowed to flow along its front surface, as shown in Figure 3a, a magnetic pressure will be imposed on the front surface of the specimen in accordance with Eq. 1. As apparent, the magnetic pressure risetime will follow the risetime of the applied current profile. Figure 3b illustrates a typical current risetime and resulting pressure history, which produces a pressure wave in the sample for these kinds of experiments on Z. The magnetic field diffuses into the sample at a rate depending on its electrical conductivity. Gradients in the magnetic pressure accelerate material giving rise to mechanical pressures. The peak magnetic pressure can be easily controlled by either choosing a geometry that results in a specific current density for a specific applied current or by controlling the applied voltage that results in the desired applied current.

Two initial configurations have been used to date that demonstrate the feasibility of using the Z Accelerator for isentropic compression experiments. These configurations are shown in Figures 4a and 4b. In the geometry shown in Figure 4a, the sample is located in the anode and directly exposed to the 2-3 mm vacuum insulating gap between the cathode and anode. In this case, the peak current density is determined by the applied peak current and the radius of the anode at the center of the sample location. Since different parts of the sample front surface have different current densities due to convergence and geometry, this configuration is not ideal for ICE measurements. It has, however, been used on two experiments with iron specimens to demonstrate feasibility of the technique for investigating polymorphic phase transitions.

Figure 4b shows a configuration that is better for ICE measurements on the accelerator, but still has some limitations. In this case, the flat sample disk is located on the surface of the cathode adjacent to the anode-cathode gap. For this situation, the current density on the surface of the anode is constant because of a fixed radius, but the sample surface has slightly different pressures imposed across its surface due to an asymmetry in the radial gap. Two experiments on copper were performed in this geometry to demonstrate the feasibility of using fast pulsed power techniques for measuring stress-volume curves. In these experiments, the diameter of the copper disks were 3.5 mm and the cathode radius was 20 mm, resulting in a maximum input stress of approximately 200 kbar. The variation in applied pressure over the sample surface is small but must be quantified in future applications with this geometry. Further improvements to the geometries shown in Figure 4 are in progress that should achieve the requirement of 0.5% uniformity in

applied magnetic pressure stated earlier. These will not be discussed in the present paper, but recent calculations and preliminary data indicate that our goal of an uniform drive will be achievable[10].

MHD effects on ICE wave propagation

It is not the intent of this paper to describe all the MHD effects in great detail. Rather, we will point out important issues that relate to our goals for ICE such as the need for the compression wave to propagate into material at a known initial state. One of the significant issues pertaining to the use of magnetic compression is how diffusion of the magnetic field and attendant joule heating affect the propagation of compression waves in the sample. Analytic expressions are given below which provide some estimates of the diffusion effect for general applications. This is followed by a more detailed discussion of numerical simulations that have been performed to address these effects.

We define magnetic-flux penetration depth, $s_\varphi(t)$, in a 1-D semi-infinite material as:

$$s_\varphi(t) = \frac{1}{B(0,t)} \int_0^\infty B(x,t)\, dx, \tag{2}$$

where B(0,t) is the B field at the surface. Assuming that the electrical resistivity of the material increases linearly with thermodynamic energy density and that the field at the boundary, B(0,t), is proportional to $t^{1/2}$, $s_\varphi(t)$ becomes

$$s_\varphi(t) = \left(\frac{5}{6\sqrt{2}}\right) \frac{B(0,t)}{B_c} \sqrt{\kappa_0 t} \tag{3}$$

from analytic non-linear magnetic-diffusion calculations[11]. B_c is the field at which the material's resistivity doubles, and κ_0 is the magnetic diffusivity.

As specific examples, for iron[11], B_c = 29 T and κ_0 = 0.071 m^2s^{-1}; for copper, B_c = 43 T and κ_0 = 0.0126 m^2s^{-1}. Using these values, it is estimated that the diffusion depths are s_φ = 0.41 mm for iron and 0.12 mm in copper at peak current, which occurs at about 100 ns. These are reasonable depths for balancing the effect of current diffusion against the requirements of sufficient sample thickness to give good accuracy in ICE measurements.

In addition to the estimates of current diffusion given above; magneto-hydrodynamic (MHD) simulations were performed with realistic resistivity models to provide more accurate time-dependent field and temperature profiles in the specimens during application of current. These calculations were performed with both the MHD codes MACH2[12-15] and Trac II[16] and a modification of WONDY. The physical processes included in the models are diffusion, Lagrangian hydrodynamics, and advection[13, 14]. The WONDY simulations are discussed in a later section on phase changes in iron.

The fidelity of the MHD calculations depends largely on an accurate knowledge of the material resistivities over a wide range of temperatures and densities. Of particular importance for these simulations is the regime defined by temperatures below a few eV and densities below solid. Reasonable electrical conductivities were estimated[17,18] for use in MACH2 and TracII which allowed meaningful simulations of field diffusion in the ICE measurements. Of particular interest was the relative diffusion of the magnetic field

and attendant joule heating, in addition to the formation of the hydrodynamic wave that propagated into the bulk of the sample. If the flux penetration rate is sufficiently fast compared to the hydrodynamic wave, the material can be pre-heated before the ICE wave arrives at a given depth.

Mach II calculations were performed for an applied magnetic field that linearly increased to 20 MA in 100 ns over the surface of a planar sample. These calculations illustrate both the diffusion of the magnetic field into the samples and the development of the mechanical stress within the sample. In this case, the samples were assumed to be a fluid, so that the longitudinal stress is actually a pressure. However, this assumption does not compromise interpretation of the results, which indicate that the mechanically generated ICE wave forms early during the loading process and propagates ahead of the magnetic field diffusion into the sample. This result is clearly apparent in Fig. 5, which shows the mechanical and magnetic responses in copper for the assumptions of constant conductivity,σ_0, and for temperature-dependent conductivity based on a modified Lee-More model[19]. Based on these calculations, the assumption that the ICE wave propagates into material at the ambient state for this loading condition in copper should be valid. This assumption has recently been confirmed experimentally and will be reported in a future publication[20].

A similar effect is observed for magnetic loading of iron under the same assumptions; these results are presented in Fig. 6. In this case, the relative time separation of the magnetic and mechanical response is smaller for a given propagation distance, making the assumption that the ICE wave propagates into ambient material less certain. The

conclusion drawn from the MHD analysis is that the hydro-wave is propagating into material with a known initial state that has not been preconditioned by field/current diffusion.

Wave Profile Measurements

The principal kinematic variable measured in the present study is the particle velocity, u_p. These measurements were made with a velocity interferometer, VISAR[21] (Velocity Interferometer System for Any Reflector), which measures the particle velocity history at a specific sample location (Lagrangian coordinate). The VISAR provides a direct measurement of particle velocity by combining Doppler-shifted light from one instant in time against reflected light from a short time, τ, later. The resulting fringe shift in the interferometer can be related to the time-resolved particle velocity, u_p, by

$$u_p(t) = \frac{\lambda F(t)}{\tau(1+\Delta\upsilon/\upsilon_0)(1+\delta)}, \qquad (4)$$

where λ is the wavelength of light used (532 nm in the present experiment), τ is the delay time of the interferometer (on the order of 0.5 ns), $\Delta v/v_0$ is the correction for light propagation in a refractive material when in-situ measurements are made at an interface between the back of the sample and a transparent material (a window). This factor is zero in the present experiments since a free surface of the sample was investigated. δ is a correction for the dispersion of the light signal in the interferometer itself as the frequency of light shifts during the measurement. For the laser frequency of light used in the present experiments, this factor is 0.034. Equation (4) allows determination of particle velocity as a function of time at the rear specimen surface.

In general, a minimum of three particle velocity profiles are required to evaluate the evolution characteristics of arbitrary waves[23]. In the special case of rate-independent wave propagation (simple waves), two particle velocity histories at different propagation distances are sufficient to determine material properties, as discussed in the following section. Since the principal objective of the present experiments was to demonstrate the magnetic loading technique, it was assumed that the flow was isentropic so only two sample thicknesses were required. For these measurements, each VISAR was coupled to the respective sample with fiber optic cables. Separate, adjacent send and receive fibers were used for this purpose, as shown in Fig. 7. Both fibers were 200 μm diameter radiation hard fibers with a 0.22 numerical aperture that were separated from the sample free surface by about 0.5 mm, without the use of lenses. These parameters result in an illuminated spot on the sample surface of about 300 μm in diameter. For the experiments reported here, the specimens had an approximately 20 nm RMS surface finish so only light rays at the appropriate reflection angle will be accepted by the receive fiber. Because the send and receive fibers are at different positions, there is a slight correction to the VISAR formula given in Eq. (4). In addition, there is not a unique reflection angle for acceptance, which may result in a loss of VISAR signal quality during surface motion. Analysis of these effects indicates that the right-hand side of Eq. (4) should be multiplied by the factor $1/\cos\theta(\ )$[22] for the present configuration, where θ is the angle between the surface normal and the center of the receive fiber[22]. In the present experiments, θ was initially 11 degrees prior to sample motion, so this factor is 1.02. With this adjustment, the reported accuracies in peak particle velocity, depending on

magnitude, are estimated to be 1-2%. It should also be noted that if the velocity is monitored for substantial times after wave arrival that the surface displacement will cause the acceptance angle to increase until the numerical aperature of the fiber excludes light from the send fiber entering the receive fiber. This effect should be accounted for in analyses of the particle velocity.

Wave Profile Analysis

When gathering Hugoniot data, a fully developed shock is generated at the time of impact, which remains constant in amplitude as it propagates throughout the sample. The conversation equations for momentum, mass, and energy (commonly referred to as the Hugoniot jump conditions[1]) can then be used to determine material properties of interest in the shocked state. Usually the shock velocity and particle velocity are measured, so the final pressure, specific volume (inverse density), and the final specific energy can be inferred. A steady shock wave propagation is shown schematically in Fig. 8a.

As previously discussed, the ICE process utilizes smoothly increasing pressure applied at the initial surface of a sample. Because of non-linear compressibility in normal materials, the risetime of the wave will decrease as it propagates, eventually forming a steady shock wave that advances with constant amplitude. As shown in Fig. 8b, it is necessary to quantitatively determine how the ICE wave evolves with propagation distance to determine the compression response of materials subjected to simple ramp waves. Our objective is to make measurements before the ramp steepens into a shock.

The analysis of arbitrary wave propagation requires detailed study of the phase velocity[23] for pressure and particle velocity. For 1-D planar loading, Aidun[23] has performed a detailed analysis of wave propagation without assuming whether the material response is isentropic or dissipative. These equations without the electromagnetic terms included, can be summarized as

$$\frac{\partial \sigma}{\partial h} = -\rho_0 \frac{\partial u_p}{\partial t} \tag{5}$$

$$\frac{\partial \varepsilon}{\partial t} = -\frac{\partial u_p}{\partial h} \tag{6}$$

$$\rho_0 \frac{\partial E}{\partial t} = -\sigma \frac{\partial u_p}{\partial h} \tag{7}$$

in Lagrangian coordinates (h, t), where equations (5-7) are conservation of momentum, mass, and energy. In these equations, σ is the longitudinal stress component taken to be positive in compression, u_p is the longitudinal particle velocity, ρ_0 is the initial density of the unstressed, ambient material, and the volumetric strain, ε , is defined in terms of the specific volume, V (=1/ρ), as $\varepsilon = 1 - V/V_0$. In Eq.(7), E is the internal energy. Non-mechanical contributions to the material response are not considered.

If rate-dependent effects are minimal, the resulting particle velocity profiles can be analyzed as simple, self-similar waves[3, 6, 7, 23]. In this specialized case, the differential form of the conservation equations can be written as

$$d\sigma = \rho_0 \, c_L(u_p) \, du_p, \quad (8)$$

$$dV = - V_0 \, du_p / c_L(u_p), \quad (9)$$

$$dE = 1/2 \, \sigma(V) \, dV, \quad (10)$$

where $c_L(u_p)$ is the Lagrangian wave velocity at a given particle velocity, u_p. The Lagrangian sound speed, at a specific pressure, is defined as the ratio of the final density to the initial density times the Eulerian sound speed. It is also defined as the initial sample thickness divided by transit time at a specific particle velocity.

To determine whether an isentropic analysis applies to any given experiment, wave profiles for at least three different propagation thicknesses must be made. In the present study, samples were studied for only two propagation distances so we assume insetropic flow and therefore, self-similar motion. Additional experiments are in progress to evaluate this assumption and will be reported in a future publication[10].

As shown in Figure 8, the ICE wave will eventually shock up at some distance, x_c. This does not occur at a unique position in the general case, since the shock jumps tend to first form at the base of the wave[3] due to our unique pressure profile available on Z. Data to use in Eqs. (8-10) must therefore be taken before the wave has shocked up.

Ideally, wave profiles should be measured in-situ without the perturbing influence of interfaces with other materials. The best accuracy using VISAR techniques is obtained, however, by measuring the interface velocities of a reflective surface between the sample of interest and a calibrated transparent material, or "laser window". It is possible to

measure wave profiles on a free surface and determine wave velocities from relative sample thicknesses, but perturbations to the measured ICE wave from a free surface are often significant. These perturbations take the form of a bending of the characteristic describing the Lagrangian wavelet at a specific pressure or particle velocity. The effect is illustrated in Fig. 9. The first wavelet, described by characteristic 1, arrives at the free surface, and causes an acceleration to twice the in-situ particle velocity, and interacts with the second wavelet after reflection. After interaction, the second wavelet propagates into a zero-pressure zone with a lower Lagrangian wave velocity, causing the wave to arrive late at the free surface by a time difference δt_2. A similar effect occurs for subsequent wavelets, with an increasing perturbed zone and associated time difference. Thus, the apparent arrival time will be too late in proportion to sample thickness, leading to apparent wave velocities that are too high, if not corrected. The deviation is larger for thinner samples because the risetime of the ICE wave is proportionately larger. When the compression wave propagates far enough for a , fully developed shock prior to arrival at the free surface, the time correction equals zero. Note that the time perturbation is both thickness- and amplitude dependent.

In general, these surface interactions are complex and difficult to quantify so the effect is best treated with a numerical simulation of the wave propagation and interaction with the free surface. The way we have chosen to estimate the error in measured wave velocity at local positions in the wave is by simulating the experiments with a 1-D wave propagation code. A wave profile was calculated at each sample free surface, the $u_{fs}/2$ approximation applied, and the profiles compared to wave profiles calculated at the same sample depth within an infinitely thick copper sample. This allows estimation of the correction term δt

shown in Fig. 9. The relationship between the corrected, or true, velocity and the measured velocity at any arbitrary value of particle velocity in the wave profile can be written as

$$c_{true} = \frac{c_{meas}}{1 + \frac{\Delta(\delta t)}{\Delta t}} \qquad (11)$$

where $\Delta(\delta t(u_p)) = \delta t_2(u_p) - \delta t_1(u_p)$.

The quantity Δt is the transit time measured directly from the free surface at the corresponding particle velocity; δt_1 and δt_2, are the corrections determined from individual wave profile simulations as depicted in Fig. 9; c_{meas} is the measured apparent Lagrangian wave velocity (difference in initial sample thickness divided by Δt) at particle velocity, u_p; and c_{true} is the corrected wave speed at the corresponding particle velocity. Once determined with numerical simulations for a specific set of experiments, the correction factor in Eq. 10 can be applied directly to the measured results. As will be shown, the correction term for ICE compression of copper to 160 kbar ranges from zero at the base of the wave to a maximum of about 2% at peak pressure. Applying this correction results in a considerably more accurate determination of wave velocity and therefore stress-volume response, as determined from Eqs. (8-10). It is possible to increase the accuracy even further by using the EOS obtained from this procedure to determine an improved EOS to use in the numerical simulations and iterate to a converged solution. Additional experiments are in progress to examine this correction process in more detail with simultaneous near-in-situ wave profile and free surface measurements being performed in aluminum[24].

Accuracy

The accuracy of determining stress-volume states from wave profile analyses depends on several factors. First, it is necessary to determine if the waves are simple or arbitrary, as discussed by Aidun[23]. Generally, this is a difficult process, requiring careful analysis of wave profiles at different propagation distances. A determination of whether the waves are simple can be made by critically comparing profiles in normalized coordinates (time divided by sample thickness) for at least three different sample thicknesses. If the measured velocity histories are identical in this scaled frame, then the waves are simple (or self-similar). Assuming that simple wave propagation applies, Eqs (8-10) can be used to analyze the wave evolution.

The experimental error in particle velocity at points in the wave is dominated mainly by the sensitivity of the VISAR and the uncertainty in refractive index changes of laser windows under compressive loading. If the VISAR record quality is good, the particle velocity at any point in the wave profile can be determined to within 2% of the fringe constant with relative ease. For ICE waves, the percentage accuracy is less at low particle velocities and better for velocities near the peak value. For the results reported in this paper, the peak particle velocity is typically known to 1-2%, depending on experimental parameters. For the copper experiment, shot Z452, the accuracy in velocity at the peak is about 1%. Since the accuracy is velocity dependent, the average accuracy corresponding to the mid-value particle velocity (2%) will be assumed in the following error discussion. If a laser window is used, the factor $\Delta v/v_0$ from Eq. (4), which relates changes in refractive index to the pressure behind the compressive wave, must also be accurately known.

The most important factor in determining accurate stress-volume states is the measurement of wave velocity at specific points in the ICE profile. Typical relative transit times for states on the particle velocity profiles of Z452 are about 70 ns. In this experiment, the sampling error in time measurement is believed to be 0.5 ns, resulting in a RMS timing error for determining uncorrected wave velocities between the two profiles of 0.7 ns. The relative difference in sample thicknesses is 317 μm, which was determined to about 2 μm. This results in a RMS error in relative sample thickness of about 0.9%. Combining the errors in transit time and sample thickness results in a RMS error of in wave velocity at points along the wave of approximately 1.4 %.

The directly determined wave velocities must also be corrected for the perturbation of the reflected wave from the free surface, as discussed previously and as illustrated in Fig. 9. This contribution to the uncertainty is material and pressure dependent. It is shown in the next section for application of the technique to copper that the correction is a maximum of 0.7% at a pressure of 75 kbar and 2% at the pressure of 160 kbar. It is estimated that the relative uncertainty from the free surface perturbation to the uncertainty of determining in-situ wave velocity is no more than about 0.5% (one quarter of the maximum calculated correction) for the 160 kbar experiment. Factoring this into the overall analysis results in 1.5% for the total uncertainty in determining wave velocity in the experiments on copper reported later in the paper.

The density of the samples studied in the present experiments is known to better than 0.1%, which results in a negligible contribution to the overall uncertainty of determining

stress and volume. Another critical factor, however, is the uncertainty in determining in-situ particle velocity from the measured free surface profiles. It was assumed that the measured free surface velocities could be converted to in-situ velocities by dividing the measured profiles by a factor of two at any point along the wave. For purely isentropic response this approach should be exact. For elastic-plastic or viscoplastic response, the factor of two approximation is not correct. Numerical simulations performed for conditions of these experiments indicate that this assumption is good to at least xx%. Thus, the total RMS error in determining stresses during the loading history is estimated to be about 2.5% (assuming 0.5% for the uncertainty due to E-P effects - this must be checked). In a similar way, the error in strain can be determined to be about 2.5% during loading. In the future, it should be possible to reduce this error to about 1-2% through more careful determination of sample thickness, use of thicker samples. better timing accuracy (it should be possible to achieve relative time differences of 100 ns and 0.1 ns accuracy in transit times), and use of laser windows to minimize reflected wave perturbations which decrease the uncertainty of determining both in-situ particle velocity and wave velocity.

The analysis above assumes that systematic errors are negligible and that the largest contribution to accuracy results from random errors. Systematic errors can arise from several sources including gradients in loading pressure across the sample surface, asymmetries in loading pressure between samples, errors in assuming isentropic response, rate-independent effects during loading, and from other sources as yet unknown. Experiments are in progress to quantify the other effects, which will be reported in a future publication.

Applications to material studies

Several experiments have been conducted on the Z Accelerator to demonstrate the feasibility of obtaining material property data from ICE waves generated in iron and copper. The general thrust of the experiments was first to demonstrate the ability to obtain isentropic EOS data on a material such as copper where the EOS is reasonably well known, and, second, to evaluate the ability to detect the known polymorphic phase transition in iron[25].

Several samples of iron and copper were studied. The parameters for these experiments are given in Table I. The specific experiments and results are discussed below.

Iron

ICE wave experiments were performed with iron to establish the feasibility of detecting the well-known bcc-hcp polymorphic phase transition[25] occurring at 130 kbar. Additional details of the experiments can be found in ref [26]. The Armco iron used in these experiments had a purity of 99.8%, an average grain size of 150 μm and a density of 7.85 g/cm^3. The samples used were from the same stock as those studied by Barker and Hollenbach[25].

The first experiment was performed with a 0.5 mm sample (shot Z 315). The second experiment was performed with two samples, each 3 mm in diameter, and with nominal thicknesses of 0.5 mm and 0.8 mm (shot Z329). The samples were located in the anode plate at a radius of 1.385 cm from the axis of symmetry, as illustrated schematically in

Fig. 4a. The current applied to the front surface of both iron specimens ramped to about 19.3 MA over 100 ns as determined from magnetic probes (B-dot probes). As discussed earlier, the current converges toward the axis of symmetry in this geometry so the current density is not constant across the loading surface of the sample. Since J varies with radius as $I/2\pi r$, Eq. (1) shows the applied magnetic pressure will vary as the inverse radius squared, thereby inducing a non-linear pressure variation estimated to be about 7% from the center of the iron specimen to a radius that could influence the VISAR record at the center. Although this variation is not acceptable for accurate EOS measurements, it is low enough in the present experiments to demonstrate the sensitivity of the technique for detecting phase transitions useful in evaluating kinetic effects.

The results obtained in the present experiments demonstrate the ability to easily detect the α - ε phase transition. The continuously evolving nature of the wave profiles can be used to estimate the kinetic effects of the phase transition. In a typical shock wave experiment it is necessary to determine kinetic effects of phase transformations by measuring the decay of the P1 wave for different experiments at different sample thicknesses. In the present experiment, the transformation kinetics can be estimated in a single experiment.

Figure 10 illustrates resulting wave profiles obtained on the free surfaces in shots 315 and 329. In shot 315, a single iron sample of nominal thickness 0.5 mm was used. In shot 329, two samples of thickness of 0.5 and 0.8 mm were used. The iron samples were polished to a surface finish of about 1 μm RMS in all cases and coupled to the VISAR, as previously described. The free surface velocity profile at 0.5 mm thickness shows an

elastic precursor followed by the onset of the α - ε phase transition, which occurs at a particle velocity of about 0.6 km/s. These features are repeated at the 0.5 mm position in the second experiment, indicating the repeatability of the technique. The wave profile for the thicker sample also shows the elastic wave, followed by a better-defined two-wave structure. The first plastic wave (referred to as the P1 wave) carries the material to the onset of the bcc-hcp polymorphic transition. The second wave (referred to as P2) effects the transformation to the high-pressure phase in the final state.

Barker and Hollenbach[25], as well as others[27], have shown that the α-ε phase transition in iron does not proceed in thermodynamic equilibrium. Rather, some of the α phase can persist as a metastable phase in the region of stability for the ε phase. In this region, the transformation progresses toward equilibrium over time scales of a few tens of nanoseconds. Whenever experimental dimensions are centimeters and experiment durations are microseconds, these kinetics are minimal for interpreting results because wave evolution is essentially over and a fully evolved, two-wave structure is observed. For the present experiment time durations of only 10's of ns, these kinetic effects dominate wave propagation in the transition region.

The non-equilibrium thermodynamics of the iron phase transition have been modeled with a non-equilibrium equation-of-state formulation that includes the effects of electromagnetic fields. All kinetic parameters of the mechanical response and diffusion of the electromagnetic field are included through a modification to a general-purpose, one-dimensional Lagrangian hydrodynamics code[28]. The equations of state for the α and

ε phases were established by Andrews[29]. We also adopted a generalization[30] of his numerical method[31], which can be summarized as follows. The pressure and temperature at each time and position are advanced using the finite difference form of the transformation matrix:

(12)

$$\begin{pmatrix} \dot{P} \\ \dot{T} \end{pmatrix} = \begin{pmatrix} -(K_{s,x} + \gamma_x q) & -\frac{\gamma_x}{V}\underline{H}\bullet + \frac{K_{s,x}}{V}\underline{V}\bullet \\ -(\gamma_x T + \frac{q V}{C_{v,x}}) & -\frac{\underline{H}\bullet}{C_{v,x}} + \frac{\gamma_x}{V} T \underline{V}\bullet \end{pmatrix} \begin{pmatrix} \frac{\dot{V}}{V} \\ \dot{\underline{x}} \end{pmatrix}$$

$$\dot{x}_i = \sum_j \frac{G_j - G_i}{\tau_{ij}}$$

where the time rate of change for pressure and temperature are expressed in terms of the rate of change of volume and mass fraction, x. Eq. (12) is simply a mathematical re-expression of the assumptions that a non-equilibrium mixture of the α and ε phases is at uniform pressure and temperature locally. All thermodynamic quantities are evaluated at fixed mass fraction, x, of the phases and are described in detail in ref. 30. In modeling the experiments, Maxwell's equations were re-formulated to make them compatible with the wave propagation calculations and solved exactly assuming constant resistivity for iron. The magnetic diffusion equation contains an additional term to account for flux compression in materials with a non-zero strain rate; gradients in the sum of the mechanical and magnetic pressure are used in the momentum equation and internal energy rises because of mechanical work, joule heating and the work done against the Lorentz force.

Figure 11 shows the experimental records obtained in shot Z329 in comparison with several 1-D numerical calculations. One of the calculations is for negligible phase transformation, i.e. the material remains in the α phase for the duration of the experiment. In this case, a single plastic wave is observed because the transformation never occurs, and the calculated result departs significantly from the experimental records. Another numerical calculation corresponds to the equilibrium transition. In this case the transition proceeds as fast as the loading demands and generates results similar to the two-wave structure observed under shock compression on thick samples[25]. As illustrated, this also disagrees with the experimental result. The best agreement with experiment is obtained for a transformation rate of about 50 μs^{-1} , which corresponds to an effective transition time of about 40 ns. This rate is in good agreement with previous measurements on the transition in iron[25].

At late times, the temperature near the front surface of the iron sample rises precipitously, invalidating the constant resistivity assumption of iron. As discussed earlier, this effect is not thought to affect the transformation rates inferred because the hydrodynamic wave propagates away from this zone prior to the precipitous heating. Further computational and experimental work is in progress to verify this assumption.

The numerical method of calculating the wave propagation requires specification of the front surface magnetic field history. We used measured profiles from B-dot probes on each experiment located in close proximity to the samples. In performing these calculations, it was found that the B-field determined from the B-dot probes used to determine the input magnetic field did not give the appropriate final loading pressure.

The second wave, P2, was too slow and the calculated peak free surface velocity never achieved the final measured value. The best fit was achieved by multiplying the measured magnetic pressure by a factor of 1.5, which implies that the magnetic field is larger than the measured field by the square root of this factor from Eq. 1. Recent 3-D MHD simulations indicate that this effect is likely due to the difference in conductivity between the pure iron samples and the stainless steel electrode or to other physical effects not yet understood. These results will be published in a future paper[10]. With this scaling, the final calculated pressure agrees more closely with B field measurements which are more likely to be accurate because they were made further away from the axis of symmetry where current densities are very high. Thus, these kinds of shock wave measurements may be valuable as an electromagnetic diagnostic for pulsed power machines.

This initial use of the ICE wave technique to detect the phase transition in iron and to obtain approximate kinetic transformation times is very encouraging. It appears to allow an easy method of detecting solid-solid and other types of transformations under dynamic loading without the problem of over-driving the transition, which often occurs in shock wave experiments. Additional experiments on iron are planned to evaluate the effects of current diffusion more carefully and to perform ICE loading under exact planar conditions.

Copper

The configuration shown in Fig. 4b was used to obtain isentropic EOS data on copper to 160 kbar. For EOS experiments, this geometry is preferable to that used on iron because

the pressure gradient is limited to the effect from a local, non-symmetrical gap between the anode and cathode caused by a 6-mm chord placed in the wall of a 40-mm diameter tube. Samples of copper were machined in the form of a cup with a precise front thickness and pressed into the stainless steel cathode to provide current contact and to eliminate the need for adhesives. The copper samples used were OFHC with a density of 8.93 g/cm^3. They were diamond turned to a 20-nm RMS finish on the parallel surfaces. VISAR interferometers were coupled to the samples using previously discussed techniques. Experimental parameters are given in Table I.

Two experiments were performed with the geometry shown in Fig. 4b. The first of these, shot Z382[33] is shown in Fig. 12a. The measured input current history is shown with units of MA on the left abscissa. As illustrated the current rises to a peak value of about 16.4 MA with an effective risetime (10-95%) of about 80 ns. From Eq. (1), note that this corresponds to a pressure interval of about 1-90%. Wave profiles are also shown with velocity coordinates on the right abscissa. The VISAR records are somewhat noisy, especially for the thicker sample because of an inadequate surface finish on the samples. This experiment was repeated in shot Z452, which is shown in Fig. 12b. The input current, which rises to about 22.4 MA, is shown on the left abscissa and the velocity on the right for nominal sample thicknesses of 0.5 mm and 0.8 mm. The VISAR signal qualities are much better for this experiment, approaching that achieved on gas guns. The effective current risetime in this experiment was also about 80 ns and the peak pressure about 160 kbar.

As expected for a material with convex stress-strain curvature, the risetime of the compressive wave decreases as is propagates from the thin to the thick sample. For shot Z452, the risetime of the plastic wave is about 40 ns at the thinner sample and less than 10 ns for the thicker. For determining the P-V response in both experiments, it was assumed that the in-situ particle velocity at any point in the wave was one half of the measured free surface velocity, u_{fs}. Computer simulations using elastic-perfectly plastic material response were performed that show this assumption is accurate for rate-independent hydrodynamic response, as discussed earlier. Elastic-perfectly plastic response is not completely representative of copper. However, the compressive yield strength of copper has been shown to increase from about 0.5 kbar at ambient conditions to approximately 5 kbar at a shock pressure of 150 kbar[32]. Assuming that a similar change applies to materials experiencing isentropic compression, computer simulations indicate that the $u_{fs}/2$ is accurate to within xx% for peak pressures of 160 kbar. This correction was not applied to the data since the exact form of the compressive strength is not known.

A first estimate of the Lagrangian wave velocity corresponding to a specific particle velocity in the wave was obtained from direct measurements of the difference in transit time between the two samples at a fixed in-situ particle velocity. This approach does not account for the perturbation to the waves near the free surface, as illustrated in Fig. 9. Using the free surface correction technique discussed earlier, a time deviation that increased from zero at the foot of the wave to a few ns at the top, was observed. This effect, which depended on sample thickness, is illustrated in Fig. 13. For the sample thicknesses used in the present experiments, the observed time deviations resulted in a

percentage error that increased from zero to 2% at the top of the wave. Dividing the apparent wave velocity by the factor one plus the correction shown in Fig. 13 (Eq. 4) results in a better approximation to the in-situ wave velocity.

The corrected wave velocities for shot Z452 are compared with isentropic sound speeds reported for copper[34] in Fig. 14. As illustrated, the agreement between the present experimental results and previously reported results is very good over the pressure range studied, indicating the accuracy of the approach for obtaining accurate in-situ wave velocities.

Stress-volume data as determined above were also obtained from shots Z382 and Z452 and are shown in Fig. 15. in comparison to previously reported Hugoniot data for copper[33-36]. Because of the less-than-optimal signal quality obtained on shot Z382, only the region in the box shown in Fig. 12a was analyzed. First, it is noted that the σ-V data from the two experiments overlay to within the experimental error bars discussed earlier, although Z382 data tends to be slightly higher. The quality of data on this shot, however, was not as good as that for Z452 so the error bars are larger. The data for Z452 also overlap Hugoniot data over the range from 70-160 kbar, although the present data lie slightly higher. Near 100 kbar, the difference between the two is about 5 kbar, which is within the error bar for both sets of data. It is useful, however, to explore the possibilities for this difference.

The deviation cannot be explained by differences in thermodynamic properties between the Hugoniot and isentrope. The theoretical difference in pressure is given by[37]

$$P_H(V) = P_S(V) + \frac{B_0\left(B_0' + 1\right)}{12}\gamma_0\varepsilon^3 + \text{ higher order terms,} \qquad (13)$$

where $P_H(V)$ is the Hugoniot function, $P_S(V)$ is the isentrope, B_0 is the adiabatic bulk modulus at ambient conditions, B_0' is its pressure derivative, γ_0 is the ambient Gruneisen ratio and ε is the volumetric strain. For copper, these values are 1386 kbar, 5 and 1.96, respectively. Using these values, the difference between the Hugoniot and the isentrope for copper at a peak pressure of 150 kbar is about 0.8 kbar, which is approximately a 0.5% correction. Thus, the pressure-volume response measured with the ICE technique and previously reported Hugoniot data in Figure 15 should agree for all practical purposes over this stress regime.

It is possible that the wave velocities are not fully corrected for the free surface perturbation. The correction approach described earlier has the effect of reducing the wave velocities and thus the slope of the stress-volume curve. If the correction factor is not accurately determined, the error in the stress-volume curve will be increased by approximately twice the error in velocity. To account for the 5 kbar difference in the pressure-volume plane would require an additional 2% correction in velocity, which is not likely based on computer simulations.

Another source of error could result from the assumption that the wave propagation in copper is rate-independent. Although this effect cannot be quantified with the present data set, rate-dependent material behavior would tend to produce a stiffer instantaneous response, followed by relaxation to the equilibrium response. This effect would accentuate the present differences. Additional experiments with several sample

thicknesses will be necessary to resolve this possibility. Other systematic errors, such as non-planar loading, could also account for differences between the two curves. This effect is presently under investigation and will be reported in a future paper[10].

A plausible explanation for the slightly stiffer-than-expected isentropic response could result from a strength effect. Chhabildas has noted that in a number of metals, in particular tungsten[7], that the continuous loading response lies above the Hugoniot curve over pressures of several hundred kbar. This behavior could be the result of micro-mechanical induced strength effects related to thermal softening during shock compression that are not present in isentropic loading. Although both the Hugoniot data and isentropic compression data in Fig. 15 include strength effects, the magnitude of the strength could be quite different due to the effects mentioned above. Since a similar discrepancy between Hugoniot and isentropic loading has been observed in several other metals, it is prudent to keep this possibility in mind in future experiments with isentropic compression.

Because the current ultimately drops, a release fan follows the compressive ramp. When the compression wave reflects from the free surface as a rarefaction wave, it meets the oncoming release fan producing a tension in the material. The result of this wave interaction is a pullback in particle velocity of about 0.07 km/s that corresponds to a spall strength of approximately 17 kbar, in agreement with reported values[38].

The initial isentropic compression data obtained on copper are very encouraging. Even though there appears to be slight disagreement between the existing Hugoniot and new

isentrope data for copper, the ability to obtain precision loading data with the present technique implies that it may be possible to probe the underlying micro-mechanical mechanisms that could account for this difference in future experiments. Resolution of the difference will require increased accuracy with the present loading, diagnostics and analysis techniques, in combination with strictly planar 1-D loading.

Work in Progress

Several developments are in progress which should substantially increase the accuracy and ease of performing ICE measurements on the Z accelerator. The major goal is to achieve 1-2% accuracy in stress-volume loading curves to pressures of about 1 Mbar. The first step in achieving this goal will be to develop a configuration on the accelerator that produces true one-dimensional planar loading of specimens. Initial experiments to achieve this goal have been encouraging and will be reported in a future publication[10]. A related goal is to study ICE loading of several samples simultaneously in order to resolve issues of rate-dependence and to increase the accuracy of measuring wave velocities. We have performed initial experiments not yet published that show the feasibility of isentropically loading eight samples simultaneously. With additional improvements, this technique will substantially reduce the cost of performing ICE measurements and will also improve the ability to measure wave evolution over many sample thicknesses to identify rate effects. We are also increasing the peak pressure possible with this technique towards 1 Mbar and the input risetime to about 200 ns, which will allow thicker samples and increased accuracy in measuring wave velocities. When these objectives are accomplished, it should be possible to make precision ICE measurements for EOS applications.

There is also a need to study low density materials and materials which may not be good electrical conductors. Studies are being conducted at present that will qualify both aluminum and copper as standard ICE drivers for use with other materials. In these configurations, it should be possible to mount samples under study on one of the drivers and perform ICE measurements without current diffusion into the sample. This approach will also allow study of non-metals and liquids to provide a broader spectrum of possible phase transition studies.

Summary

In this paper, a new experimental technique is discussed which can produce smoothly increasing compression on metallic samples to pressures of several hundred kbar. The method uses magnetic fields produced by the Z Accelerator at Sandia National Laboratories to produce continuous pressure loading of planar samples over time scales of about 100 ns. For rate-independent materials, with low strength, this loading history produces isentropic material response which approximates the behavior of many real materials; hence the method is referred to as the Isentropic Compression Experiment.

The ICE technique has been combined with traditional shock diagnostics to allow measurement of dynamic material response for these loading conditions. The ramp waves produced in this technique are measured at different thicknesses of samples subjected to continuous loading over 100 ns. Analysis of these wave profiles allows approximation of the high-pressure isentrope in the material under study.

The method has been applied to the study of iron and copper in order to demonstrate feasibility of obtaining EOS and phase transformation data with this technique. Iron has a pressure-induced phase transition from bcc to hcp that initiates at 130 kbar. ICE experiments conducted on iron demonstrate the ability to easily detect this transition and to also determine the transformation kinetics in one experiment. Traditionally, several shock wave experiments are necessary to obtain similar data. ICE experiments conducted on copper show that it is possible to determine the continuous loading response of this material to about 160 kbar in a single experiment. The resulting quasi-isentropic curve is in good agreement with previously published shock compression data on copper. Typically, shock compression data requires several experiments to obtain the same data that can be obtained in a single isentropic compression experiment. Both of these feasibility demonstrations illustrate the potential for using this method in studies of dynamic material response.

* Sandia is a multiprogram laboratory operated by Sandia Corporation, a Lockheed Martin Company, for the United States Department of Energy under Contract DE-AC04-94AL85000.

Acknowledgements

We would like to acknowledge the many people who have contributed to the development of this technique, including the operations team on the Z Accelerator. Special thanks are due to Mike Bernard who has been instrumental in developing many of the diagnostic techniques used to implement ICE on Z; Lynn Barker, who conceived many of the original ideas for isentropic compression experiments; Dillon McDaniel who

has provided many ideas about fast pulsed techniques for this application; and Lalit Chhabildas, who was instrumental in developing many of the techniques for using gas guns to perform ICE experiments.

References

1. J.R. Asay and G.I. Kerley, *Int'l J. Impact Eng'g*, 5 69-99 (1987).
2. M.R. Boslough and J.R. Asay, Basic Principles of Shock Compression , in High-Pressure Shock Compression of Solids, ed. by James R. Asay and Mohsen Shahinpoor, Springer-Verlag, New York, (1993).
3. L.M. Barker, SHOCK WAVES IN CONDENSED MATTER – 1983, J.R. Asay, R.A. Graham, G.K. Straub, ed., Elsevier Sci. Publ, B.V., 217 (1984).
4. L.M. Barker and R.E. Hollenbach, *J. Appl. Phys.* **41**, 4208-4226 (1970).
5. L.M. Barker, Bull. Amer. Phys. Soc. 20, 1498 (1974).
6. J.R. Asay and L.C. Chhabildas, HIGH PRESSURE SCIENCE & TECH., ed. by B. Vodar and Ph. Marteau, Pergamon Press, Vol. 2, 958-965 (1980).
7. L.C. Chhabildas and L.M. Barker, SHOCK WAVES IN CONDENSED MATTER – 1987, S.C. Schmidt, N.C. Holmes, editors, Elsevier Sci. Publ, B.V. 111-114 (1988).
8. R. Hawke, D.E. Duerre, J.G. Huebel, J.G. Klapper, D.J. Steinberg and R.N. Keeler, *J. Appl. Phys.* 43, 2734-2741 (1972).
9. M.K. Matzen, *Phys. Plasmas.* 4 (5), 1519- 1527 (1996).
10. D. Reisman, et al. (to be published, 2000).
11. H. Knoepfel, *Pulsed High Magnetic Fields*, North Holland Publishing Company, London, UK, 1970.
12. S.E. Rosenthal, M. P. Desjarlais, R. B. Spielman, W. A. Stygar, J. R. Asay, M. R. Douglas, C. A. Hall, M. H. Frese[1], R. L. Morse[2], and D. B. Reisman, " MHD Modeling of Conductors at Unltra-high Current Density, proceedings of the 12th IEEE International Pulsed Power Conference, Monterey, CA, June 1999. Submitted for publication in IEEE Transactions in Plasma Science.

[1] NumerEx, Inc, Albuquerque, NM
[2] University of New Mexico, Albuquerque, NM

13. MACH Reference Manual by R. E. Peterkin, Jr. and M. H. Frese, July 1998. The code must not be distributed without written permission from the Air Force Research Laboratory: Phillips Research Site, Kirtland AFB, NM.

14. M. H. Frese, "MACH2: A Two-Dimensional Magnetohydrodynamic Simulation Code for Complex Experimental Configurations", AMRC-R-874, Mission Research Corporation, 1987.

15. M. H. Frese, Mission Res. Corp. No. AMRC-R-874, unpublished (1987).

16. D. B. Reisman, "Numerical simulation of fiber and wire array Z-pinches with Trac-II", UCRL-LR-131742, Lawrence Livermore National Laboratory, 1998.

17. A. W. DeSilva and J. D. Katsouros, Phys. Rev. E **57**, 5945 (1998).

18. G.A. Rinker, Phys. Rev. A **37**, 1284 (1988).

19. Y.T. Lee and R.M. More, Phys. Fluids **27**, 1273 (1984).

20. J.E. Bailey et al., determination of field diffusion in copper samples, to be published (2000).

21. L.M. Barker and R.E. Hollenbach, *J. Appl. Phys.* **43**, 4669 (1972).

22. J.B. Aidun and Y.M. Gupta, *J. Appl. Phys.* **69**, 6998-7014 (1991).

23. L.C. Chhabildas and J.W. Swegle, J. Appl. Phys., **51**, 4799-4807 (1980).

24. C.A. Hall, et al., to be published (2000).

25. L.M. Barker and R.E. Hollenbach, *J. Appl. Phys.* **45**, 4872-4887 (1974).

26. J.R. Asay, C.A. Hall, K.G. Holland, M.A. Bernard, W.A. Stygar, R.B. Spielman, S.E. Rosenthal, D.H. McDaniel, D.B. Hayes, "Isentropic Compression of Iron with the Z Accelerator", Proceedings of the American Physical Society Topical Group on Shock Compression of Condensed Matter, Snow Bird, Utah, June 26 - July 2, 1999 (to be published).

27. J.C. Jamieson and A.W. Lawson, *J. Appl. Phys.* **33**, 776 (1962).

28. M.E. Kipp and R.J. Lawrence, SAND REPORT, No. 81-0930, Sandia National Laboratories, unpublished (1981).

29. D.J. Andrews, *J. Phys. Chem. Solids*, **34**, 825-840 (1973).

30. D.B. Hayes, *J. Appl. Phys.*, **46**, 3438 (1975).

31. D.J. Andrews, *J. Comp. Phys.* **7**, 310 (1971).

32. J.R. Asay Proceedings of the American Physical Society Topical Group on Shock Compression of Condensed Matter, Snow Bird, Utah, June 26 - July 2, 1999 (to be published).

33. L.C. Chhabildas, and J.R. Asay, HIGH PRESSURE IN RESEARCH AND INDUSTRY, ed. By C. M. Backman, T. Johannisson and L. Tegner, Vol. 1, 183-187 (1982).

34. R.G. McQueen, S.P. Marsh, J.W. Taylor, J.N. Fritz, and W.J. Carter, "The Equation of State of Solids from Shock Wave Studies", in **High Velocity Impact Phenomena**, ed. by Ray Kinslow, Academic Press, New York (1970).

35. Walsh, J.M. M.H. Rice, R.G. McQueen, F.L. Yarger, Phys. Rev. **108** (2), 196-216, (1957)

36. Marsh, S.P., editor, LASL Shock Hugoniot Data, University of California Press, (1980)

37. G.E. Duvall and B.J. Zwolinski, *Acoust. Soc. Am.*, **27**, 1054-1058 (1955).

38. Copper spallation data.

FIGURE CAPTIONS

Fig. 1. Relationship between isotherms, Hugoniots and isentropes in a fluid.

Fig. 2. Z accelerator used to produce current loading over time intervals of 100-200 ns. The accelerator is about 30 m in diameter, with a central target chamber of about 3m in diameter where the current from the thirty six modules of the machine converges on axis.

Fig. 3 Conceptual diagram showing how magnetic loading can be used to produce material loading on metallic specimens exposed to the magnetic field. (a) location of a sample in a conducting material resulting in an applied magnetic stress on the sample. (b) typical current and pressure histories produced in the sample.

Fig. 4 Two configurations used to produce magnetic loading on planar specimens placed in the anode or cathode of the Z accelerator. (a) location of planar cylindrical specimens

shown at a specific radius in a converging geometry of the cathode. (b) location of a planar specimen placed at a specific radius on an annular anode.

Fig. 5. Evolution of the hydrodynamic wave and the diffusion of the magnetic field and current for a 100 ns current risetime to 20 megamps superposed on the surface of a copper specimen.

Fig. 6. Evolution of the hydrodynamic wave and the diffusion of the magnetic field and current for a 100 ns current risetime to 20 megamps superposed on the surface of a iron specimen.

Fig. 7. Schematic of the configuration used to couple laser light reflected from the target to the VISAR systems.

Fig.8. Evolution of waves in compressed materials. (a) steady shock wave propagation. (b) ICE wave propagation; formation of a shock occurs at x_c .

Fig. 9 Effects of wave perturbation at the interface between a sample and another material or free surface.

Fig. 10. (a) VISAR particle velocity profile obtained on a 0.5 mm thick sample of iron at a peak pressure of 300 kbar (Z315). (b) VISAR profiles obtained on 0.5 and 0.8 mm thick iron samples at peak pressures of about 300 kbar (Z329).

Fig. 11. Comparison of numerical simulations and experimental measurements of ICE wave evolution in iron.

Fig. 12. Particle velocity profiles for ICE wave propagation in copper specimens. (a) shot Z382, 0.5 and 0.8 mm thick specimens. (b) shot Z452, 0.5 and 0.8 mm thick specimens. In both figures the current profile is shown with coordinates on the left abscissa and the particle velocity profiles with coordinates on the right abscissa.

Fig. 13. Correction factor for an initial 100 ns ICE wave reflecting from the free surface of a 0.5 mm thick copper sample.

Fig. 14. Comparison of experimentally determined wave velocities with reported isentropic velocities.

Fig. 15. Stress-volume curves produced by isentropic loading of copper to different final pressures and comparison with previously published Hugoniot results.

Table I. Parameters for ICE wave Experiments

Exp't	Config.	Sample	Sample Dim.	Material	Current	Peak

No.	(fig. No.)	No.	Dia. X Thk, mm		density* Mamps/cm	Pressure Kbar
Z315	4a	1	3.0 X 0.508	Iron	1.92	319
Z329	4a	1	3.5 X 0.506	Iron	1.88	346
		2	3.5 X 0.793	Iron		296
Z382	4b	1	3.5 X 0.604	Copper	1.33	107
		2	3.5 X 0.914	Copper		74
Z452	4b	1	9.0 X 0.491	Copper	1.78	201
		2	9.0 X 0.808	Copper		

* Based on current measurements from Bdots probes placed near the load.

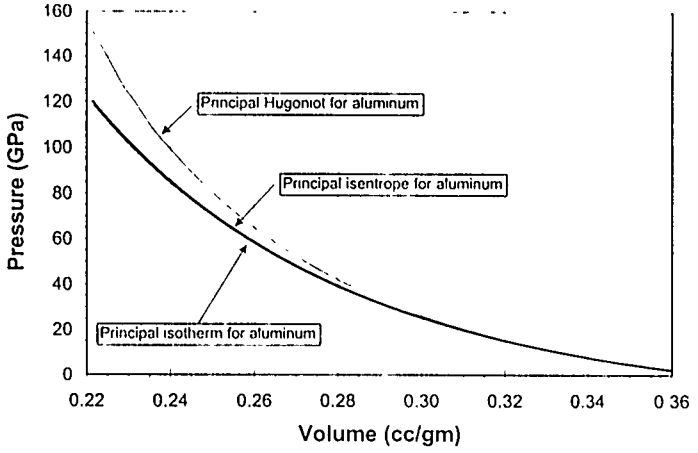
160
140
120
100
80
60
40
20
0
Pressure (GPa)
Principal Hugoniot for aluminum
Principal isentrope for aluminum
Principal isotherm for aluminum
0.22
0.24
0.26
0.28
0.30
0.32
0.34
0 36
Volume (cc/gm)

Figure 1

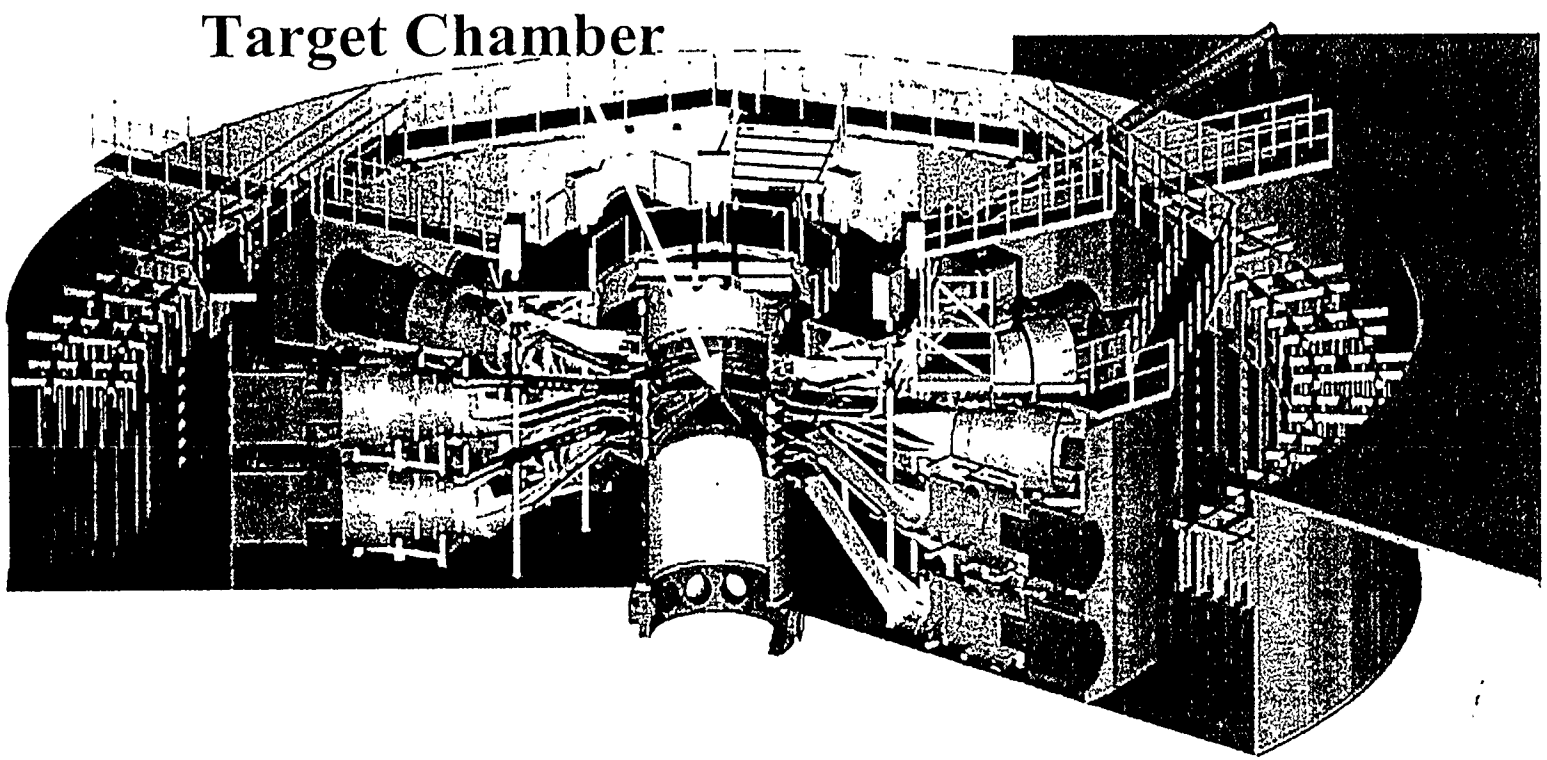

Figure 2

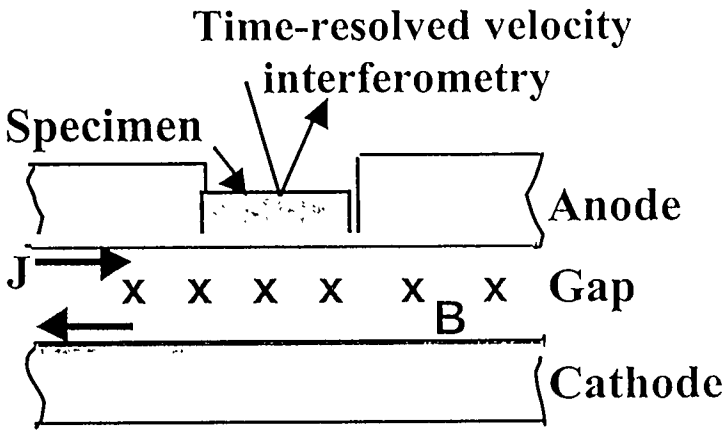
Time-resolved velocity
interferometry
Specimen
Anode
J
x x x x x x
B
Gap
Cathode

(a)

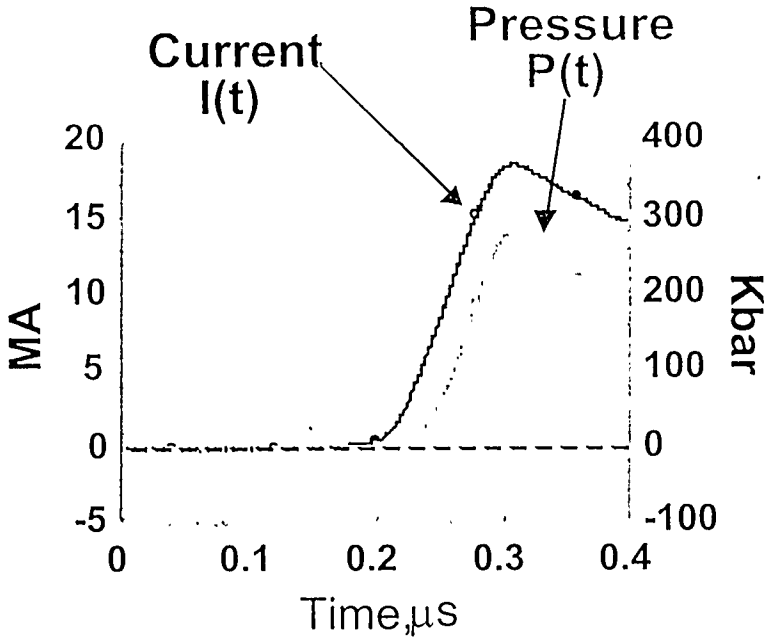
Current
I(t)
Pressure
P(t)
MA
Kbar
20
15
10
5
0
-5
400
300
200
100
0
-100
0
0.1
0.2
0.3
0.4
Time,μs

(b)

Figure 3

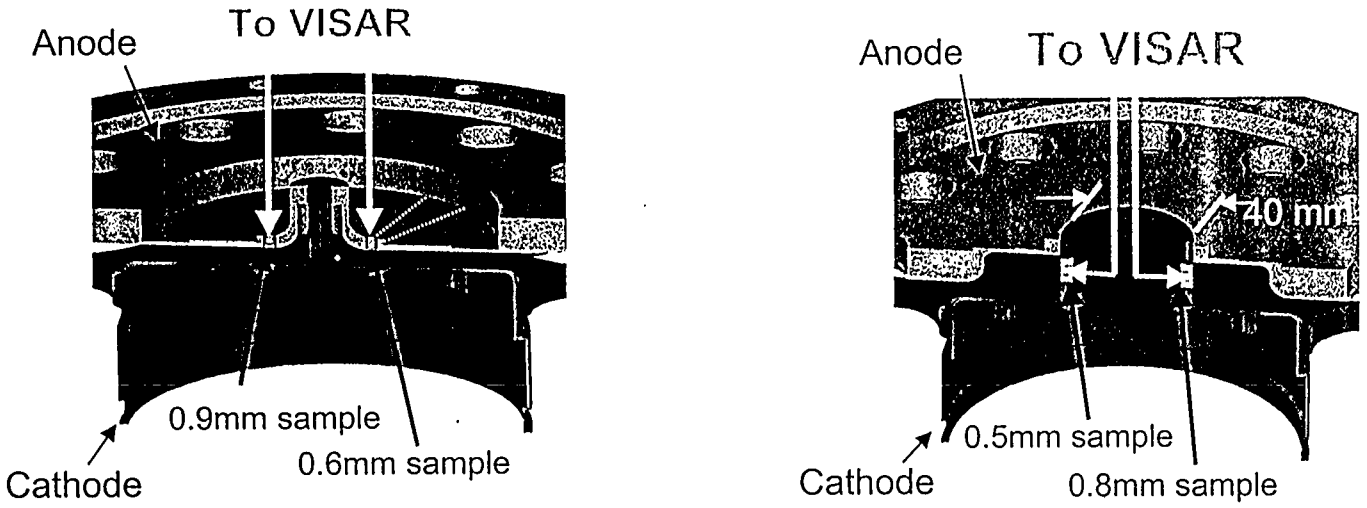
Anode
To VISAR
0.9mm sample
0.6mm sample
Cathode
(a)
Anode
To VISAR
40 mm
0.5mm sample
0.8mm sample
Cathode
(b)

Figure 4

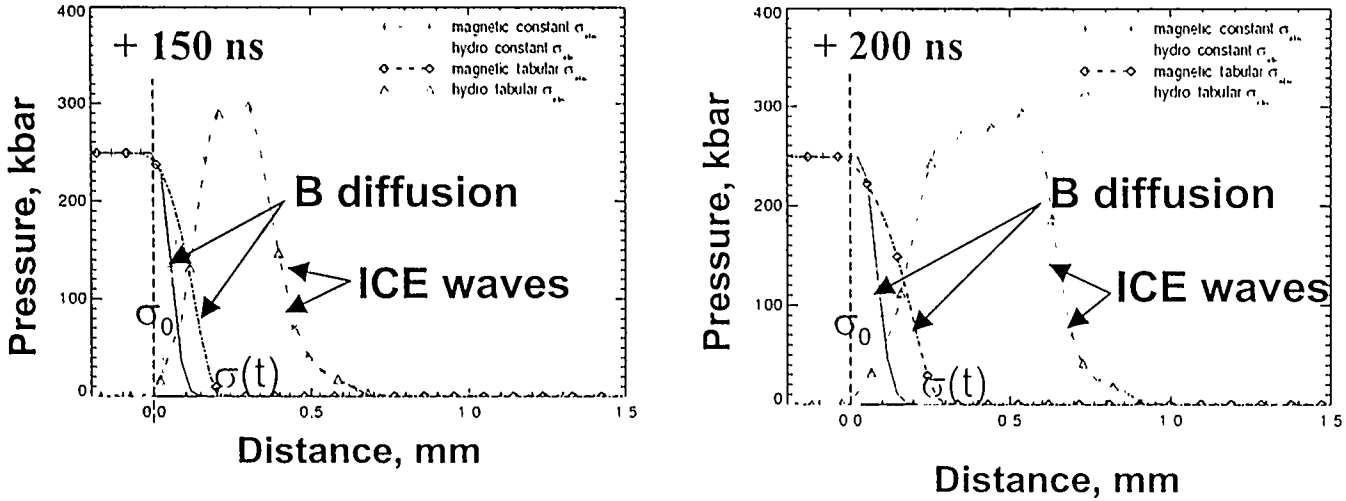
+ 150 ns
magnetic constant
hydro constant
magnetic tabular
hydro tabular
B diffusion
ICE waves
σ_0
$\sigma(t)$
Pressure, kbar
Distance, mm
400
300
200
100
0
0.0
0.5
1.0
1.5

+ 200 ns
magnetic constant
hydro constant
magnetic tabular
hydro tabular
B diffusion
ICE waves
σ_0
$\sigma(t)$
Pressure, kbar
Distance, mm
400
300
200
100
0
0.0
0.5
1.0
1.5

Figure 5

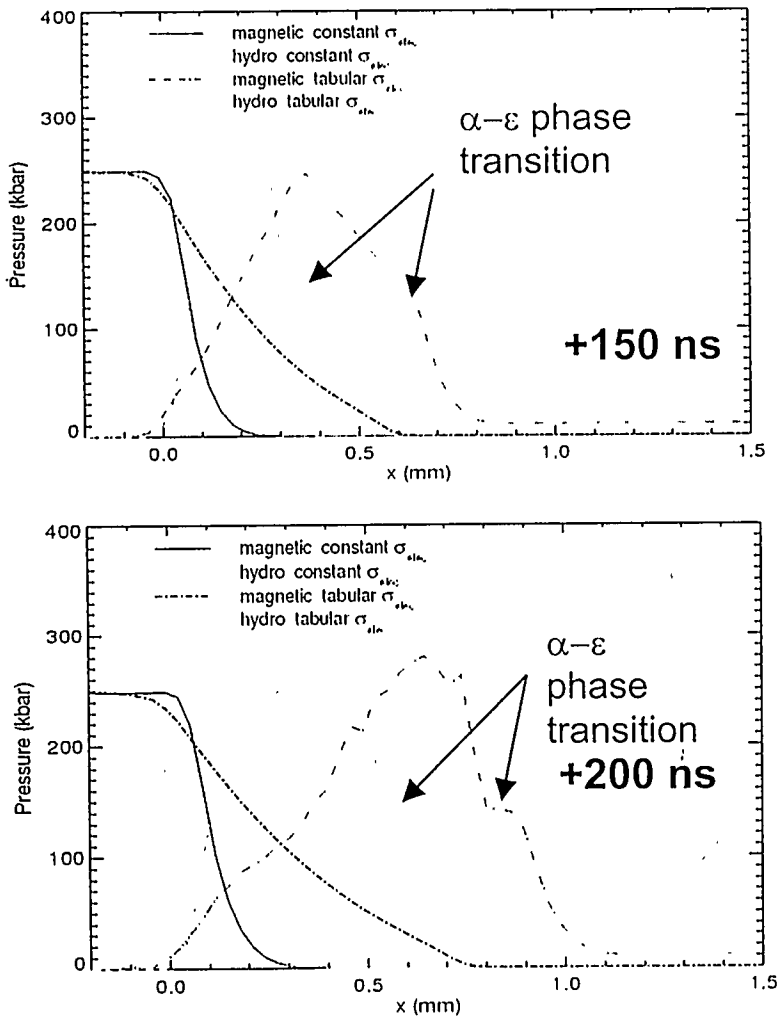
magnetic constant σ
hydro constant σ
magnetic tabular σ
hydro tabular σ
α–ε phase transition
+150 ns
Pressure (kbar)
x (mm)
0
100
200
300
400
0.0
0.5
1.0
1.5
magnetic constant σ
hydro constant σ
magnetic tabular σ
hydro tabular σ
α–ε phase transition
+200 ns
Pressure (kbar)
x (mm)

Figure 6

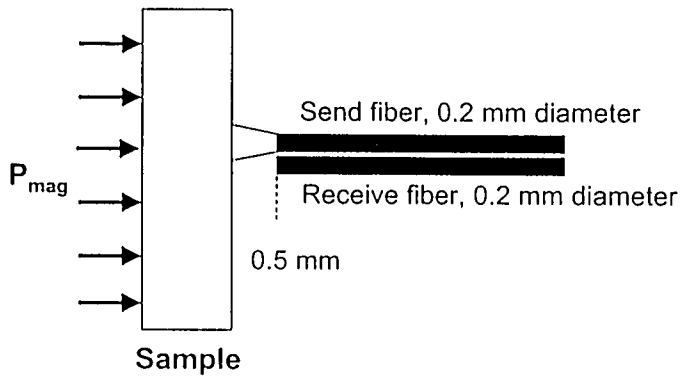
Send fiber, 0.2 mm diameter
P_{mag}
Receive fiber, 0.2 mm diameter
0.5 mm
Sample

Figure 7

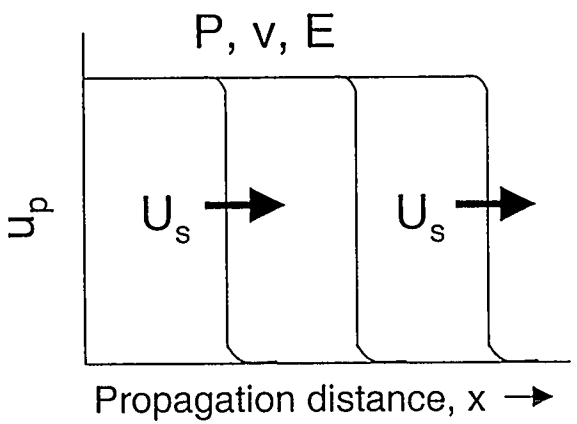

Steady Shock:
measure U_s and u_p

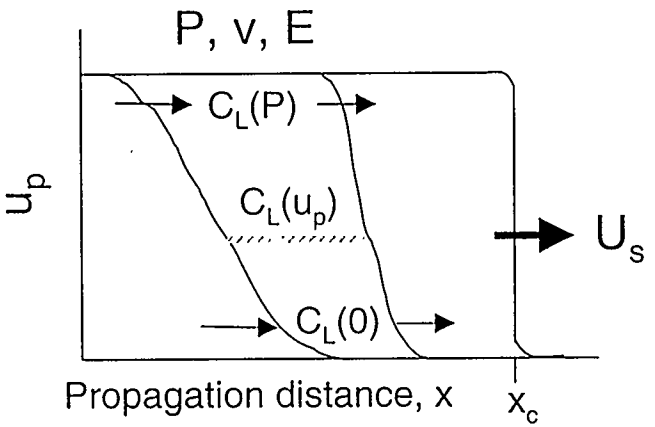

ICE wave:
measure $C_L(u_p)$

Figure 8

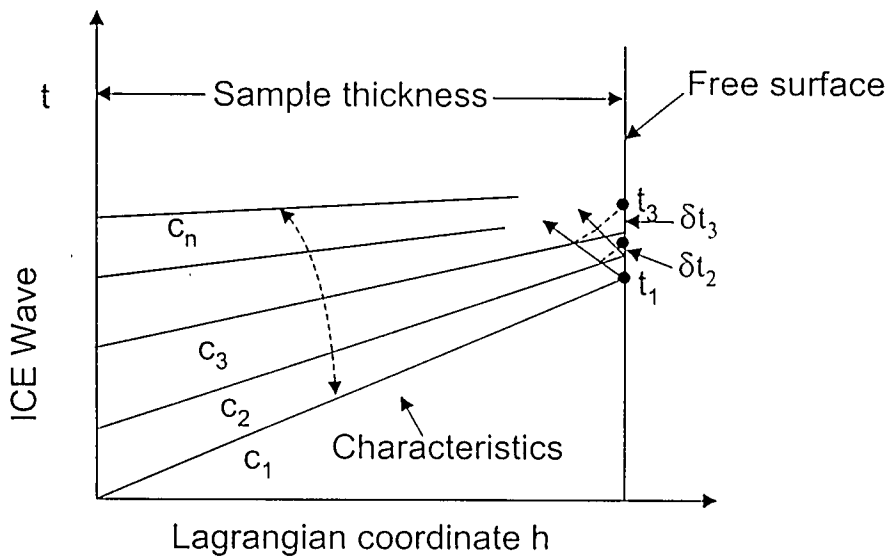
t
Sample thickness
Free surface
t_3
δt_3
δt_2
t_1
c_n
c_3
c_2
c_1
Characteristics
ICE Wave
Lagrangian coordinate h

Figure 9

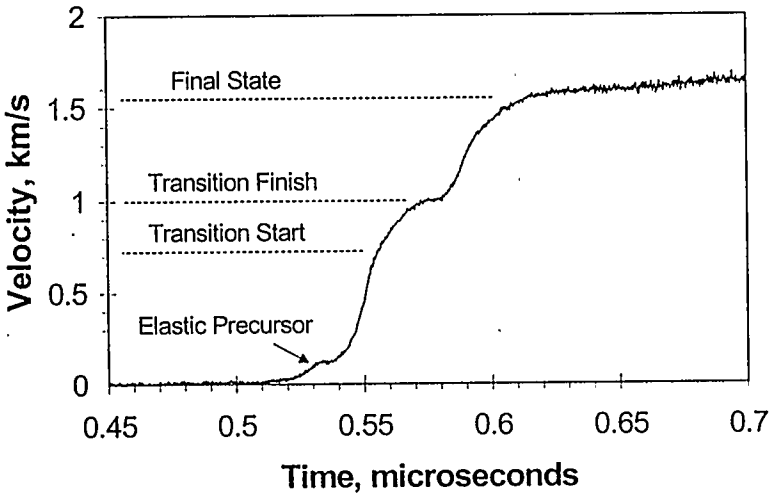
Final State
Transition Finish
Transition Start
Elastic Precursor
Velocity, km/s
Time, microseconds
0
0.5
1
1.5
2
0.45
0.5
0.55
0.6
0.65
0.7

(a)

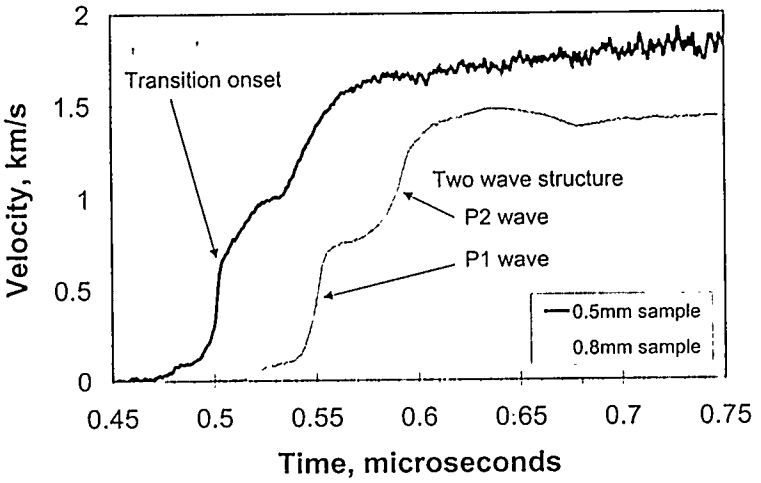
Transition onset
Two wave structure
P2 wave
P1 wave
0.5mm sample
0.8mm sample
Velocity, km/s
Time, microseconds
0
0.5
1
1.5
2
0.45
0.5
0.55
0.6
0.65
0.7
0.75

(b)

Figure 10

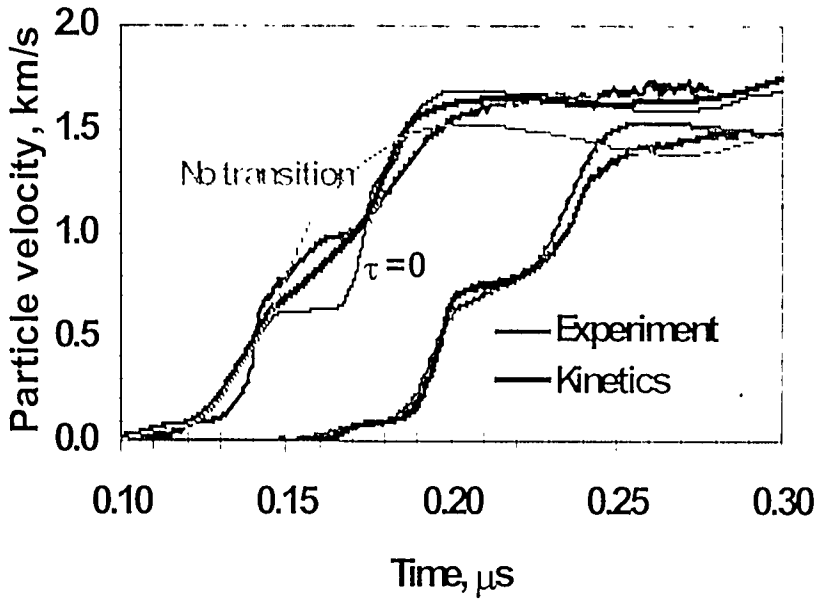
Particle velocity, km/s
2.0
1.5
1.0
0.5
0.0
No transition
τ = 0
Experiment
Kinetics
0.10
0.15
0.20
0.25
0.30
Time, μs

Figure 11

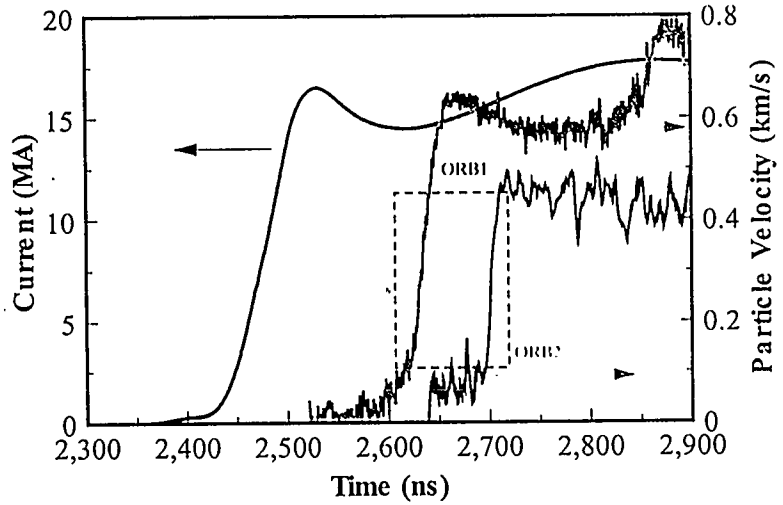
Current (MA)
Particle Velocity (km/s)
Time (ns)
ORB1
ORB2
20
15
10
5
0
0.8
0.6
0.4
0.2
0
2,300
2,400
2,500
2,600
2,700
2,800
2,900

(a)

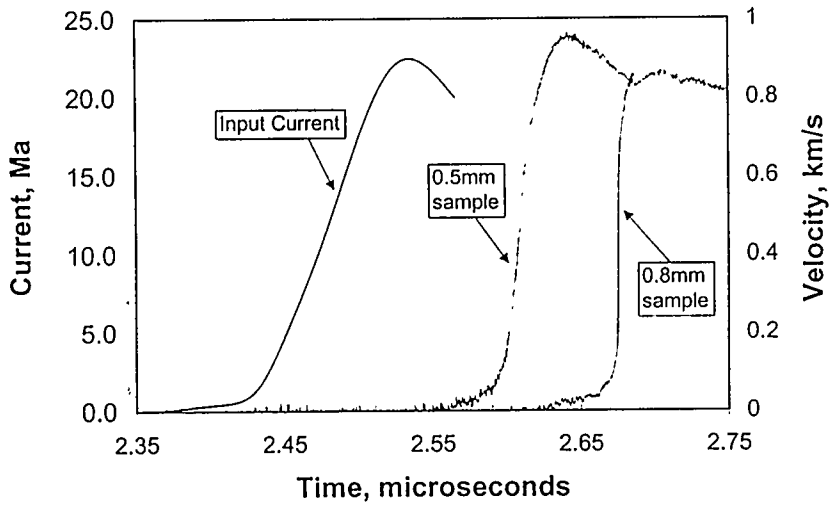
Current, Ma
Velocity, km/s
Time, microseconds
Input Current
0.5mm sample
0.8mm sample
25.0
20.0
15.0
10.0
5.0
0.0
1
0.8
0.6
0.4
0.2
0
2.35
2.45
2.55
2.65
2.75

(b)

Figure 12

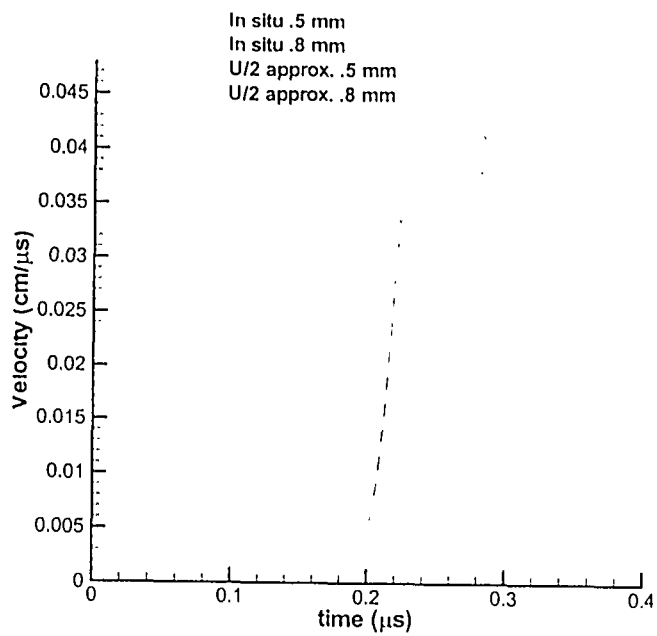
In situ .5 mm
In situ .8 mm
U/2 approx. .5 mm
U/2 approx. .8 mm
Velocity (cm/μs)
0.045
0.04
0.035
0.03
0.025
0.02
0.015
0.01
0.005
0
0
0.1
0.2
0.3
0.4
time (μs)

Figure 13

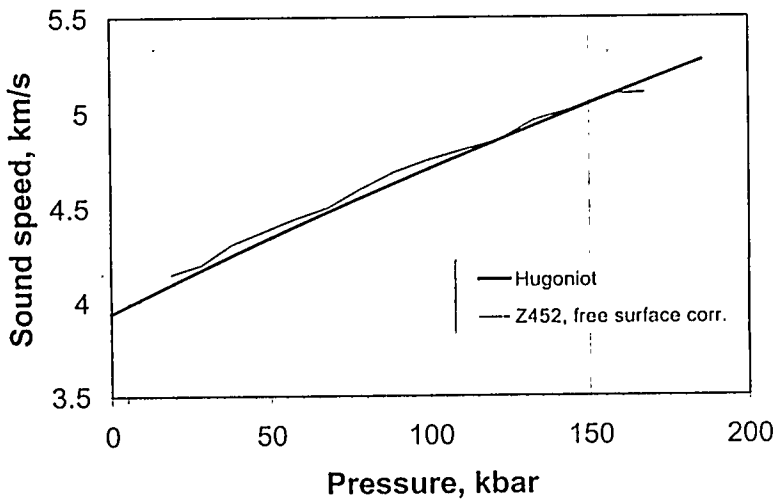
5.5
5
4.5
4
3.5
Sound speed, km/s
0
50
100
150
200
Pressure, kbar
Hugoniot
Z452, free surface corr.

Figure 14

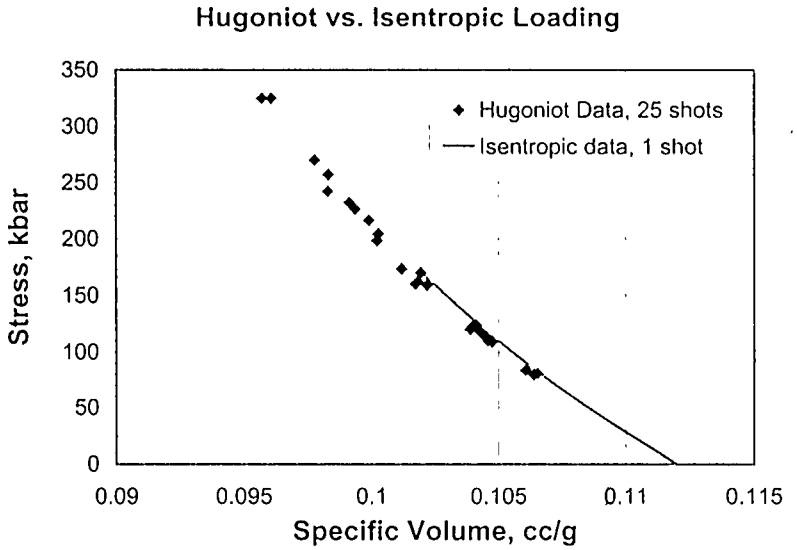
Hugoniot vs. Isentropic Loading
Hugoniot Data, 25 shots
Isentropic data, 1 shot
Stress, kbar
350
300
250
200
150
100
50
0
0.09
0.095
0.1
0.105
0.11
0.115
Specific Volume, cc/g

Figure 15